PHYSICAL REVIEW D **96,** 043008 (2017)

# Rotating hybrid stars with the Dyson-Schwinger quark model

J.-B. Wei (魏金标) and H. Chen (陈欢)[*]
*School of Mathematics and Physics, China University of Geosciences, Lumo Road 388, 430074 Wuhan, China*

G. F. Burgio and H.-J. Schulze
*INFN Sezione di Catania, Via Santa Sofia 64, 95123 Catania, Italy*
(Received 27 March 2017; published 15 August 2017)

We study rapidly rotating hybrid stars with the Dyson-Schwinger model for quark matter and the Brueckner-Hartree-Fock many-body theory with realistic two-body and three-body forces for nuclear matter. We determine the maximum gravitational mass, equatorial radius, and rotation frequency of stable stellar configurations by considering the constraints of the Keplerian limit and the secular axisymmetric instability, and compare with observational data. We also discuss the rotational evolution for constant baryonic mass and find a spin-up phenomenon for supramassive stars before they collapse to black holes.

DOI: 10.1103/PhysRevD.96.043008

## I. INTRODUCTION

Neutron stars (NS) are among the densest objects known in the Universe. They contain an extreme environment shaped by the effects of the four fundamental interactions. NS have a typical mass $M \sim 1.4\ M_\odot$ and radius $R \sim 10$ km. Therefore, the mean particle density can reach $(2–3)\rho_0$, and the core density $\sim 10\rho_0$ [1–5], where $\rho_0 = 0.17\ \mathrm{fm}^{-3}$ is the so-called nuclear saturation density. At this density, the nucleons might undergo a phase transition to quark matter (QM), and a hybrid NS (HNS) with a QM core is formed [6,7]. This makes NS ideal astrophysical laboratories to study hadronic interactions over a wide range of densities [8].

Unfortunately, as a key ingredient of the investigation of NS, the equation of state (EOS) remains uncertain. The microscopic theory of the nucleonic EOS has reached a high degree of sophistication [1,9–22], but the QM EOS is poorly known at zero temperature and at the high baryonic density appropriate for NS, because it is difficult to perform first-principle calculations of QM.

Therefore one can presently only resort to more or less phenomenological models for describing QM, such as the MIT bag model [23], the Nambu–Jona-Lasinio model [24–27], the quasiparticle model [28,29], or the quark-meson model [30]. Dyson-Schwinger equations (DSE) provide a nonperturbative continuum field approach to QCD that can simultaneously address both confinement and dynamical chiral symmetry breaking [31,32]. In Refs. [33–35] we developed a Dyson-Schwinger quark model (DSM) for deconfined QM based on the DSE formalism, which was combined with a Brueckner-Hartree-Fock (BHF) approach for the hadronic phase in order to model NS. In those works, we considered static and spherical symmetric HNS, whereas in this paper we include the effects of rotation.

(Fast) rotation and related phenomena of NS could be important features in the sense that they might eventually allow us to deduce properties of the underlying EOS, e.g., the question of whether or not QM is present in the interior of NS. Several phenomena have been proposed in this regard, e.g., the possible existence of "twin" NS configurations with the same mass but different radii [36–41], the "backbending" or spin-up phenomenon caused by the onset of the quark phase [42,43], or the onset of the phase transition and associated energy release in decelerating fast pulsars [42–45].

Rotation is a common property of NS. Of the thousands of currently observed pulsars, the fastest one has been discovered in the globular cluster Terzan 5 with a frequency of 716 Hz [46]. At this rapid rotation, a NS would be flattened by the centrifugal force, and the Tolman-Oppenheimer-Volkoff equation, suitable for a static and spherically symmetric situation, cannot describe correctly the rotating stellar structure. In the present paper we approximate the NS as an axisymmetric and rigid rotating body, and resort to Einstein's theory of general relativity for a rapidly rotating star. Numerical methods for an (axisymmetric) rotating stellar structure have been advanced by several groups [47–51]. In this work we utilize the KEH method [47] to obtain the properties of rapidly rotating HNS.

This paper is organized as follows. In Sec. II we briefly discuss the construction of the EOS of a HNS. In Sec. III we present the rotation effects on the HNS; the allowed ranges of gravitational mass, equatorial radius, and Kepler frequency are discussed in this section and compared with observational data. The rotational evolution for a constant baryonic mass is also analyzed. Section IV contains our conclusions.

[*]huanchen@cug.edu.cn

 

## II. THE EQUATION OF STATE

### A. Nuclear matter

For nuclear matter we resort to the BHF many-body theory with realistic two-body and three-body nucleonic forces, which has been extensively discussed in Ref. [52]. We recall that this theory has also been extended with the inclusion of hyperons, which might appear in the core of a NS. The hyperonic EOS turns out to be very soft, and this results in too low NS maximum masses [53], well below the current observational limit of about two solar masses [54–56]. The presence of strange baryonic matter also often inhibits the appearance of QM [57]. In this work we do not discuss this aspect, but limit ourselves to consider only nucleons and leptons in the hadronic phase.

In the BHF theory the energy per nucleon of nuclear matter is given by

$$\frac{B}{A}=\frac{3}{5}\frac{k_F^2}{2m}+\frac{1}{2\rho}\sum_{k,k'<k_F}\langle kk'|G[e(k)+e(k');\rho]|kk'\rangle_A, \quad (1)$$

where $G[W;\rho]$ is the solution of the Bethe-Goldstone equation

$$G[W;\rho]=V+\sum_{k_a,k_b>k_F}V\frac{|k_a,k_b\rangle Q\langle k_a,k_b|}{W-e(k_a)-e(k_b)}G[W;\rho], \quad (2)$$

$V$ is the bare nucleon-nucleon (NN) interaction, $\rho$ is the nucleon number density, and $W$ the starting energy. The single-particle energy

$$e(k)=e(k;\rho)=\frac{k^2}{2m}+U(k;\rho) \quad (3)$$

and the Pauli operator $Q$ determine the propagation of intermediate baryon pairs. The BHF approximation for the single-particle potential using the *continuous choice* is

$$U(k;\rho)=\sum_{k'\le k_F}\langle kk'|G[e(k)+e(k');\rho]|kk'\rangle_A. \quad (4)$$

Due to the occurrence of $U(k)$ in Eq. (3), the above equations constitute a coupled system that has to be solved in a self-consistent manner for several momenta of the particles involved, at the considered densities. The only input quantities of the calculation are the NN two-body potentials. In this work we present results obtained with the Bonn-B (BOB) potential [58] as input, supplemented with compatible three-body forces [16,59,60]. The associated EOS yields fairly large maximum masses of about 2.5 $M_\odot$ for purely nucleonic NS (NNS).

For the calculation of the energy per nucleon of asymmetric nuclear matter, we use the so-called parabolic approximation [11],

$$\frac{B}{A}(\rho,x)=\frac{B}{A}(\rho,x=0.5)+(1-2x)^2E_{\rm sym}(\rho), \quad (5)$$

where $x=\rho_p/\rho$ is the proton fraction and $E_{\rm sym}(\rho)$ is the symmetry energy, which can be expressed in terms of the difference of the energy per nucleon of pure neutron matter ($x=0$) and symmetric matter ($x=0.5$):

$$E_{\rm sym}(\rho)=\frac{B}{A}(\rho,x=0)-\frac{B}{A}(\rho,x=0.5). \quad (6)$$

The parametrized results of pure neutron and symmetric matter with different interactions can be found in Ref. [16]. The energy density of baryon/lepton matter as a function of the different partial densities is then

$$\varepsilon(\rho_n,\rho_p,\rho_e,\rho_\mu)=(\rho_n m_n+\rho_p m_p)+(\rho_n+\rho_p)\frac{B}{A}(\rho_n,\rho_p)+\varepsilon_e(\rho_e)+\varepsilon_\mu(\rho_\mu), \quad (7)$$

where $\varepsilon_e(\rho_e)$ and $\varepsilon_\mu(\rho_\mu)$ are the energy densities of electrons and muons. Once the energy density is known, the chemical composition of the beta-equilibrated matter can be calculated and finally the EOS,

$$P=\rho^2\frac{d}{d\rho}\frac{\varepsilon(\{\rho_i(\rho)\})}{\rho}=\rho\frac{d\varepsilon}{d\rho}-\varepsilon. \quad (8)$$

### B. Quark matter

The quark propagator based on the Dyson-Schwinger equation at finite quark chemical potential $\mu$ assumes a general form with rotational covariance,

$$S(p;\mu)^{-1}=i\boldsymbol{\gamma p}+i\gamma_4(p_4+i\mu)+m_q+\Sigma(p;\mu) \quad (9)$$

$$\equiv i\boldsymbol{\gamma p}A(p^2,p\cdot u)+B(p^2,p\cdot u)+i\gamma_4(p_4+i\mu)C(p^2,p\cdot u), \quad (10)$$

where $m_q$ is the current quark mass, $u=(\mathbf{0},i\mu)$, and possibilities of other structures, e.g., color superconductivity [61–63], are disregarded. The quark self-energy can be obtained from the gap equation,

$$\Sigma(p;\mu)=\int\frac{d^4q}{(2\pi)^4}g^2(\mu)D_{\rho\sigma}(p-q;\mu)\times\frac{\lambda^a}{2}\gamma_\rho S(q;\mu)\frac{\lambda^a}{2}\Gamma_\sigma(q,p;\mu), \quad (11)$$

where $\lambda^a$ are the Gell-Mann matrices, $g(\mu)$ is the coupling strength, $D_{\rho\sigma}(k;\mu)$ the dressed gluon propagator, and $\Gamma_\sigma(q,p;\mu)$ the dressed quark-gluon vertex at finite chemical potential.

For the quark-gluon vertex and the gluon propagator we employ the widely used "rainbow approximation" [33,64],

$$\Gamma_\sigma(q,p;\mu)=\gamma_\sigma, \tag{12}$$

and assume the Landau gauge form for the gluon propagator, with an infrared-dominant interaction modified by the chemical potential [33,65]

$$g^2(\mu)D_{\rho\sigma}(k,\mu)=4\pi^2 d\frac{k^2}{\omega^6}e^{-\frac{k^2+\alpha\mu^2}{\omega^2}}\left(\delta_{\rho\sigma}-\frac{k_\rho k_\sigma}{k^2}\right). \tag{13}$$

The various parameters can be obtained by fitting meson properties and chiral condensate in vacuum [66,67], and we use $\omega=0.5$ GeV, $d=1$ GeV$^2$. The phenomenological parameter $\alpha$ represents a reduction (screening) of the effective interaction with increasing chemical potential. This parameter cannot yet be fixed independently and its value has been amply discussed in previous works [33–35].

Knowing the quark propagator, the EOS of cold QM can be obtained via the momentum distribution [33,64,68],

$$f_q(|\boldsymbol{p}|;\mu)=\frac{1}{4\pi}\int_{-\infty}^{\infty}dp_4\mathrm{tr}_D[-\gamma_4 S_q(p;\mu)], \tag{14}$$

$$\rho_q(\mu)=6\int\frac{d^3p}{(2\pi)^3}f_q(|\boldsymbol{p}|;\mu), \tag{15}$$

$$P_q(\mu_q)=P_q(\mu_{q,0})+\int_{\mu_{q,0}}^{\mu_q}d\mu\rho_q(\mu). \tag{16}$$

The total density and pressure for pure QM are given by summing the contributions of all flavors. In addition, we define the phenomenological bag constant

$$B_{\mathrm{DS}}\equiv-\sum_{q=u,d,s}P_q(\mu_{q,0}), \tag{17}$$

which corresponds to the bag constant of the MIT bag model in the limit $\alpha\to\infty$. In this work we set it to a reasonable value $B_{\mathrm{DS}}=90$ MeV fm$^{-3}$ ($B_{\mathrm{DS}}^{1/4}\approx 160$ MeV); see the discussion in [33–35]. We remark that in our approach $B_{\mathrm{DS}}$ cannot be smaller than about 50 MeV fm$^{-3}\approx$ (140 MeV)$^4$, which poses the lower limit for the stability of ordinary 2QM nuclear matter [35]. These are typical values used also in other quark models [30,38].

### C. Construction of the hybrid star EOS

In order to study the properties of a rapidly rotating HNS, we should first construct the EOS of the star. In principle the EOS should be calculated in a unified consistent way from the same theory. However, the treatment of baryonic correlations in the DSE is still quite rudimentary [69–73], and therefore we resort to the usual separate modeling of the hadronic and quark phase within different theoretical approaches. Both phases are then joined by a thermodynamic phase transition.

We assume that the hadron-quark phase transition is of first order, and perform the Gibbs construction [74], thus imposing that nuclear matter and QM are beta stable and globally charge neutral. This is at variance with the Maxwell construction, where the two phases must be separately charge neutral. However, in our approach the Maxwell construction produces instable stellar configurations at the onset of the QM phase; see [33]. We remark that recently [36–41] an exotic scenario with an unstable mass gap and existence of stable twin NS configurations was proposed. However, that requires very special conditions (extremely stiff hadronic EOS giving very large NS radii, and a very strong first-order Maxwell construction to QM), which are not features of our EOSs; see also a recent discussion in [30].

We also recall that Maxwell and Gibbs constructions are the extremes of the generalized Gibbs construction taking into account finite-size effects [1,74–76], which are however currently quantitatively unknown due to missing input information. Therefore neither pure Maxwell nor pure Gibbs constructions are expected to be realized in nature.

In the purely nucleonic phase, which consists of baryons ($n$, $p$) and leptons ($e$, $\mu$), the conditions of beta stability and charge neutrality can be expressed as

$$\mu_n-\mu_p=\mu_e=\mu_\mu, \tag{18}$$

$$\rho_p=\rho_e+\rho_\mu, \tag{19}$$

where $\mu_i$ are the chemical potentials and $\rho_i$ the particle number densities. Similarly the pure QM phase, which contains three-flavor quarks ($u$, $d$, $s$) and leptons ($e$, $\mu$), should satisfy the constraints of beta stability and charge neutrality:

$$\mu_u+\mu_e=\mu_u+\mu_\mu=\mu_d=\mu_s, \tag{20}$$

$$\frac{2\rho_u-\rho_d-\rho_s}{3}-\rho_e-\rho_\mu=0. \tag{21}$$

According to the Gibbs construction, there is a mixed phase where the hadron and quark phases coexist, and both phases are in equilibrium with each other [1]. This can be expressed as

$$\mu_i=b_i\mu_B-q_i\mu_e,\qquad p_H=p_Q=p_M, \tag{22}$$

where $b_i$ and $q_i$ denote baryon number and charge of the particle species $i=n,p,u,d,s,e,\mu$ in the mixed phase. To solve those equations, we also need the global charge neutrality condition

$$\chi\rho_c^Q+(1-\chi)\rho_c^H=0, \tag{23}$$

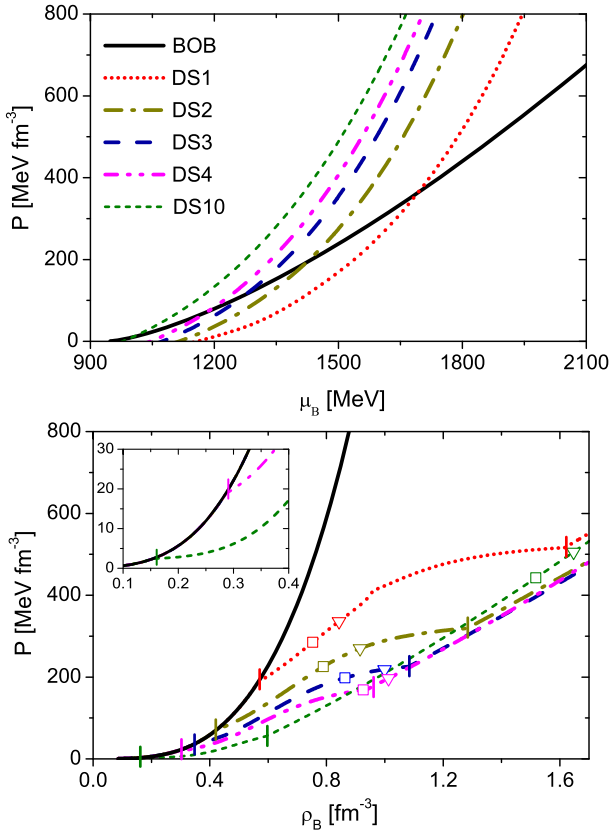


FIG. 1. Upper panel: Pressure vs baryon chemical potential for beta-stable and asymmetric nuclear matter and QM. The solid curve denotes nuclear matter using the BOB EOS, and the broken curves labeled DS$\alpha$ represent the DSM EOS for different choices of $\alpha$. Lower panel: Complete EOS of HNS with the Gibbs phase transition construction. The lower and upper limits of the mixed phase (bars) as well as the central densities of maximum-mass HNS configurations (triangles nonrotating, squares at Kepler frequency; see Table I) are marked.

where $\rho_c^Q$ and $\rho_c^H$ are the charge densities of quark and nuclear matter, and $\chi$ is the volume fraction occupied by QM in the mixed phase. From these equations, we can derive the energy density $\varepsilon_M$ and the baryon density $\rho_M$ of the mixed phase as

$$\varepsilon_M = \chi\varepsilon_Q + (1-\chi)\varepsilon_H, \tag{24}$$

$$\rho_M = \chi\rho_Q + (1-\chi)\rho_H. \tag{25}$$

In the upper panel of Fig. 1 we show the pressure vs baryon chemical potential $\mu_B = \mu_n = \mu_u + 2\mu_d$. The solid black curve represents the calculation for beta-stable and asymmetric nuclear matter with BOB EOS; the curves labeled DS$\alpha$ are for pure QM with several choices of the phenomenological parameter $\alpha$. In the lower panel the complete EOSs of HNS are shown, i.e., pressure vs baryon density. We can see that the EOS contains three sections: a pure hadronic phase at low density, followed by a mixed phase, and a pure quark phase at high density. We note that the onset of the phase transition is determined by the value of the parameter $\alpha$; larger $\alpha$ produces an increasingly softer QM EOS with a lower phase transition onset density. For high values of $\alpha$ we find that QM appears quite early, e.g., for $\alpha = 10$ at a baryon density $\rho < \rho_0$.

For completeness, we mention that for the calculation of the stellar structure we use the EOSs by Feynman *et al.* [77] and Baym *et al.* [78] for the outer and inner crusts, respectively.

## III. RESULTS AND DISCUSSION

The structure of a rapidly rotating NS is different from the static one, since the rotation can strongly deform the star. We assume NS are steadily rotating and have axisymmetric structure. Therefore the space-time metric used to model a rotating star can be expressed as

$$ds^2 = -e^{\gamma+\rho}dt^2 + e^{2\beta}(dr^2 + r^2d\theta^2) + e^{\gamma-\rho}r^2\sin^2\theta(d\phi - \omega dt)^2, \tag{26}$$

where the potentials $\gamma, \rho, \beta, \omega$ are functions of $r$ and $\theta$ only. The matter inside the star is approximated by a perfect fluid and the energy-momentum tensor is given by

$$T^{\mu\nu} = (\varepsilon + p)u^\mu u^\nu - pg^{\mu\nu}, \tag{27}$$

where $\varepsilon$, $p$, and $u^\mu$ are the energy density, pressure, and four-velocity, respectively. In order to solve Einstein's field equation for the potentials $\gamma, \rho, \beta$, and $\omega$, we adopt the KEH method [47] and use the public RNS code [79] for calculating the properties of a rotating star.

### A. Keplerian limit

The rotational frequency is a directly measurable quantity of pulsars, and the Keplerian (mass-shedding) frequency $f_K$ is one of the most studied physical quantities for rotating stars [30,40,49,80–84]. In Fig. 2 we show the gravitational NS mass as a function of the central baryon density (left panel) and of the equatorial radius (right panel), using the EOSs displayed in Fig. 1. Results are plotted for both the static configurations (thin curves) and for the ones rapidly rotating at Keplerian frequency (bold curves).

In all cases the maximum masses of HNS are lower than those of NNS, because the appearance of QM in the core of the star results in a softening of the very hard nucleonic EOS. Comparing Keplerian and static sequences, rotations increase the maximum mass and equatorial radius substantially. The maximum masses of the static and Keplerian sequences with various EOSs, as well as the corresponding equatorial radii and central densities, are listed in Table I. The maximum masses increase by about 20% from the static to the Keplerian sequence. According to the current

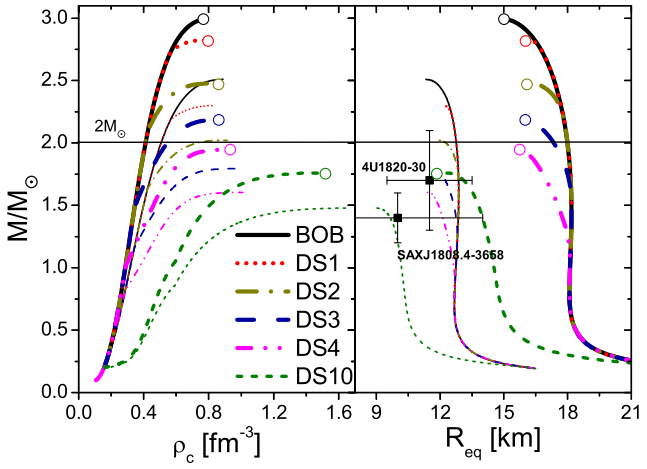


FIG. 2. Gravitational mass (in units of the solar mass $M_\odot = 2 \times 10^{33}$ g) vs the central baryon density (left panel) and vs equatorial radius (right panel) for different EOSs. Thin (bold) curves denote static (Keplerian) sequences. The end points of Keplerian sequences are marked by open circles, with properties listed in Table I. The observational data are discussed in Sec. III B.

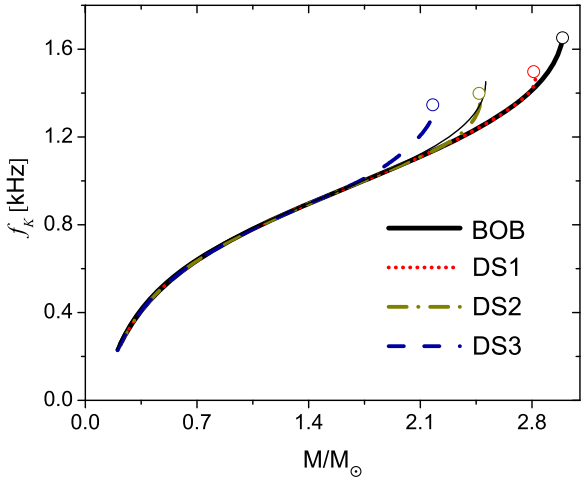


FIG. 3. Precise (bold curves) and approximated [thin solid curve according to Eq. (28)] values of Keplerian frequency vs the gravitational mass for NNS (BOB) and HNS (DS$\alpha$).

observations of massive pulsars [54–56], the DSM EOSs with $\alpha \gtrsim 2$ are ruled out. (The frequencies of PSR J1614-2230 [54,56] and PSR J0348+0432 [55] are 317 Hz and 26 Hz, respectively, which are both too small to substantially increase the maximum mass due to rotation.) In Table I we list also the densities at the lower and upper boundaries of the mixed phase, and it can be seen that a pure quark phase cannot be reached in the HNS under the constraint of $M_{\max} > 2\ M_\odot$.

In Fig. 3 we present the Keplerian frequency as a function of gravitational mass for some selected EOSs. We observe that it increases monotonically both for NNS and HNS. The Keplerian frequency of HNS increases more rapidly after QM onset, and is larger than the one of a NNS with the same gravitational mass, because the stellar radius is smaller in the former case due to the presence of a very dense QM core. However, due to the lower maximum mass of HNS, the maximum Keplerian frequency of HNS is lower than the one of NNS, as also listed in Table I for the various EOSs discussed above. Our results satisfy the constraint from the observed fast-rotating pulsar PSR J1748-2446ad with 716 Hz [46] or the even more severe constraint from XTE J1739-285 with 1122 Hz [85], which has not been confirmed, however.

We compare our results with the empirical formula

$$f_K = f_0 \left(\frac{M}{M_\odot}\right)^{\frac{1}{2}} \left(\frac{R_s}{10\ \text{km}}\right)^{-\frac{3}{2}}, \tag{28}$$

proposed in [86], where $M$ is the gravitational mass of the Keplerian configuration, $R_s$ is the radius of the nonrotating configuration of mass $M$, and $f_0$ is a constant, which does not depend on the EOS. In Ref. [83] an optimal prefactor

TABLE I. Several properties of static and rotating NS for the selected EOSs: maximum gravitational mass $M_{\max}$, corresponding equatorial radius $R_{\rm eq}$, central baryon density $\rho_c$, and the maximum Keplerian frequency $f_K$, together with the approximate value $f_{\max}$ according to Eq. (29). The lower and upper boundaries $\rho_1$, $\rho_2$ of the Gibbs mixed phase are also reported.

| EOS | | BOB | DS1 | DS2 | DS3 | DS4 |
|---|---|---|---|---|---|---|
| Static | $M_{\max}/M_\odot$ | 2.51 | 2.30 | 2.02 | 1.79 | 1.60 |
| | $R_{\rm eq}$ (km) | 11.32 | 12.13 | 11.95 | 11.72 | 11.38 |
| | $\rho_c$ (fm$^{-3}$) | 0.887 | 0.843 | 0.915 | 0.999 | 1.013 |
| Keplerian | $M_{\max}/M_\odot$ | 2.99 | 2.82 | 2.47 | 2.19 | 1.95 |
| | $R_{\rm eq}$ (km) | 14.83 | 16.17 | 16.28 | 16.00 | 15.74 |
| | $\rho_c$ (fm$^{-3}$) | 0.768 | 0.753 | 0.789 | 0.863 | 0.927 |
| | $f_K$(Hz) | 1653 | 1461 | 1399 | 1346 | 1316 |
| | $f_{\max}$(Hz) | 1641 | 1419 | 1360 | 1319 | 1257 |
| Mixed phase | $\rho_1$ (fm$^{-3}$) | | 0.566 | 0.425 | 0.340 | 0.287 |
| | $\rho_2$ (fm$^{-3}$) | | 1.617 | 1.284 | 1.081 | 0.938 |

$f_0 = 1080$ Hz in the range $0.5\ M_\odot < M < 0.9 M_{\rm max}^{\rm static}$ was obtained. Rotating HNS with masses in that range are characterized by a purely nucleonic phase, and therefore the empirical formula cannot be applied. This is at variance with NNS configurations. As displayed in Fig. 3, our results for NNS below 2.1 $M_\odot$ can be fitted well with the same parameter $f_0 = 1080$ Hz, as shown by the thin curve.

A further interesting empirical formula for the absolute maximum of the Kepler frequency for a given EOS is [43]

$$f_{\rm max} = 1220\ {\rm Hz}\left(\frac{M_{\rm max}^{\rm stat}}{M_\odot}\right)^{\frac{1}{2}}\left(\frac{R_{M_{\rm max}^{\rm stat}}}{10\ {\rm km}}\right)^{-\frac{3}{2}}. \quad (29)$$

In Table I we also list the corresponding values for our selected EOSs and observe a fair agreement within a few percent with the numerical results.

### B. Stability analysis

In order to complete the description of Figs. 2 and 3, one should pay attention to the stability criteria of stars. It is well known that the onset of the instability of the static sequence is determined by the condition $dM/d\rho_c = 0$, i.e., the curve should stop at its mathematical maximum, which thus gives the maximum mass of the static stable sequence. In the rotating case, the above criterion has to be generalized; i.e., a stellar configuration is stable if its mass $M$ increases with growing central density for a fixed angular momentum $J$ [2]. Therefore the onset of the instability, which is called secular axisymmetric instability (SAI), is expressed by

$$\left.\frac{\partial M}{\partial \rho_c}\right|_J = 0. \quad (30)$$

The configurations in the Keplerian sequences shown in Fig. 2 have different angular momenta, and thus the curves do not stop at the mathematical maximum. In the upper panel of Fig. 4 we show, for some selected EOSs, the gravitational mass for the Keplerian sequence vs the angular momentum (solid black curves), along with the SAI condition, Eq. (30), represented by the dashed red curves. Thus the Keplerian sequence should stop at the intersection with the SAI curves, which is indicated by an open circle. This constraint determines the corresponding end points of the curves in Figs. 2 and 3.

Some enlarged details are shown in the insets of Fig. 4. For a given mass $M$, there are two possible values of angular momentum $J$, which correspond to two possible values of radius $R$ in Fig. 2. In the case of NNS with the BOB EOS, the branch with the lower $R$ has larger values of $J \sim MR^2 f_K$, because the Kepler frequency $f_K$ increases faster than $R^2$ diminishes on the Keplerian sequence. In the case of HNS, the situation is opposite: the branch with the lower $R$ has also a lower value of $J$. Therefore for NNS the Kepler curve meets the SAI at large $R$, before it reaches

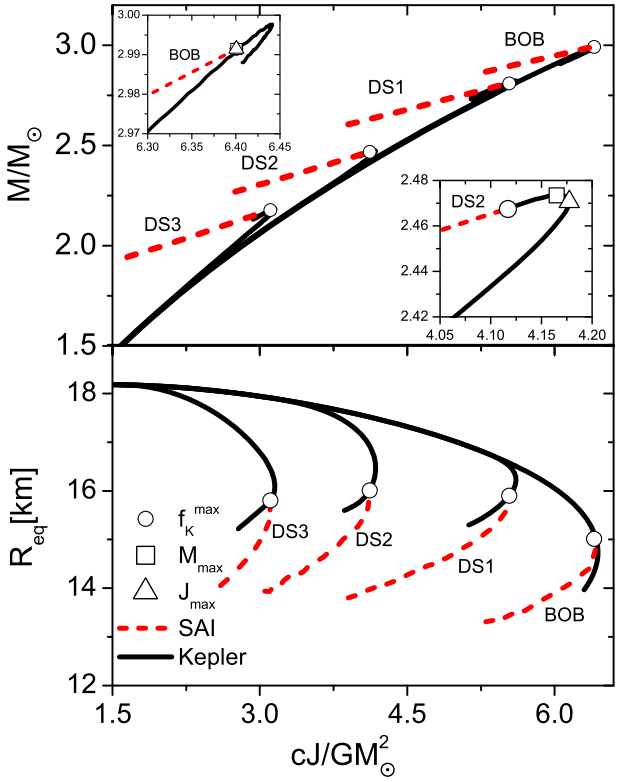


FIG. 4. Gravitational mass (upper panel) and radius (lower panel) vs angular momentum of the Keplerian sequence (solid black curves) and SAI (dashed red curves) for some selected EOSs. The open circles represent the SAI onset on the Keplerian sequence.

the mathematical maximum of the mass. This is different from the case of HNS, whose curves extend a little further on the unstable branch after they reach their mathematical maximum, before meeting the SAI, and thus the maximum mass of the stable configurations coincides with the mathematical maximum value. The maximum mass and maximum angular momentum, as well as the end point given by the SAI constraint, are obtained with different stellar configurations, and are labeled by the open squares, triangles, and circles, respectively. The discussed effects are however very small, of the order of 0.01 $M_\odot$ at most.

In order to visualize better the intricate relations among $M$, $R$, and $f_K$, we present in Fig. 5 the mass-radius relations of NS with EOS BOB (upper panel) and DS2 (lower panel) at various fixed rotation frequencies (dashed-dotted olive curves). The stable configurations are constrained by the Kepler and SAI conditions at large and small radius, respectively. At a low frequency ($f = 480$ Hz for HNS), the lower boundary of $M$ is fixed by the Kepler condition and the upper boundary by the SAI condition. As the frequency increases ($f = 796$, 1082, 1194 Hz), the SAI mark point moves more and more to the left side of the mathematical maximum (MaM), and the upper boundary of $M$ is now fixed by the MaM, which is larger than the mass

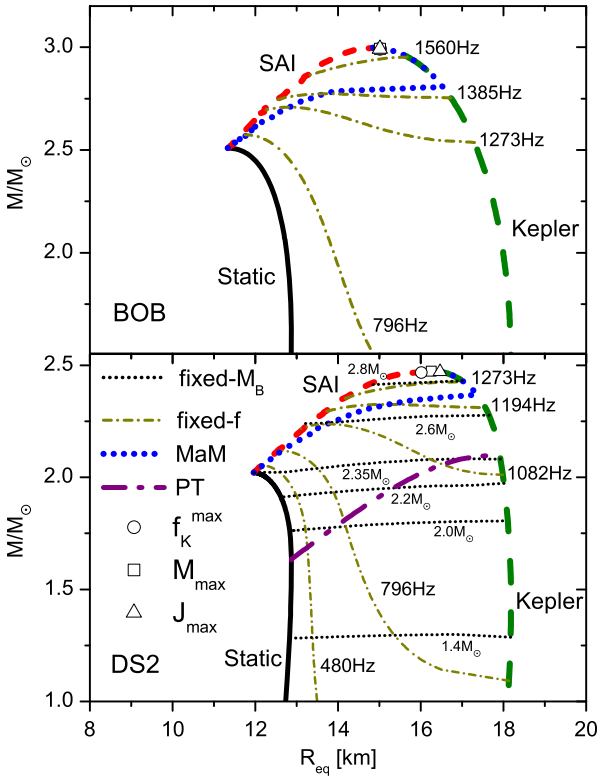


FIG. 5. Mass-radius relations of NS with the EOS BOB (upper panel) and DS2 (lower panel) at various fixed rotation frequencies $f$ (dashed-dotted olive curves) or fixed baryonic mass $M_B$ (dotted black curves, discussed with Fig. 9). The positions of the maxima of the fixed-$f$ curves are joined by the dotted blue curves. The dashed-dotted lilac line (PT) indicates the onset of the quark phase with the DS2 EOS.

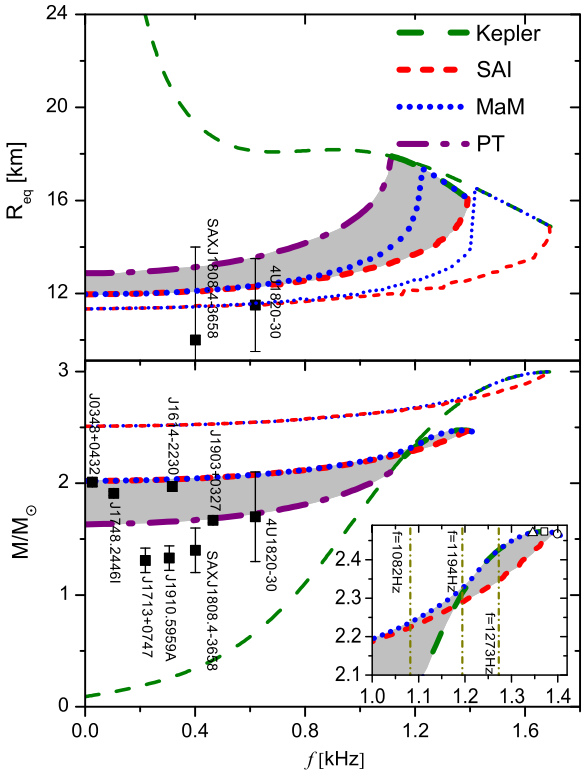


FIG. 6. The possible values of equatorial radius (upper panel) and gravitational mass (lower panel) of NS for the EOS DS2 (bold curves) and BOB (thin curves), respecting the mass-shedding (dashed green lines) and SAI limits (short-dashed red lines). The maximum-mass curves of Fig. 5 are also shown (MaM, dotted blue lines). The dashed-dotted lilac line (PT) indicates the onset of the quark phase with the DS2 EOS. The markers represent observational data [87].

at the SAI radius. This is indicated by the dotted blue curve that passes through the MaMs for fixed frequency. As the frequency increases further ($f = 1273$ Hz), the lower (upper) boundary values of $M$ are fixed by the SAI (Kepler) conditions. Finally, at the maximum frequency the Kepler and SAI conditions meet at the same point.

In Fig. 6 we present the allowed domain of NNS and HNS in the $R_{\rm eq}$–$f$ plane (upper panel) and the $M$–$f$ plane (lower panel), together with some observational data. We use the same conventions as in Fig. 5, i.e., dotted blue curves, dashed green curves, and short-dashed red curves represent the MaM, mass-shedding, and SAI limits. The allowed region of HNS with the DS2 EOS is the grey area delimited by the dashed-dotted lilac curve (PT), which represents the onset of the phase transition. One interesting feature we should mention here is that at high rotation frequency the mass range is small, while the range of radii is still large, corresponding to a flat top of the $M(R)$ curves in Fig. 2. This means the radii are very sensitive to the mass at high rotating frequency.

As discussed above, the current observations on pulsar masses constrain our parameter to $\alpha < 2$; hence we present the results of HNS with the EOS DS2. For smaller $\alpha$ the corresponding (shaded) area of HNS will shrink and move towards the lower (upper) boundary of NNS in the upper (lower) panel. The minimum (maximum) mass of HNS with EOS DS2 is 1.68 (2.02)$M_\odot$ in the static sequence, and increases as the rotation frequency increases, while the range concentrates to a single value 2.47 $M_\odot$ at the maximum frequency $f = 1.4$ kHz. Therefore, in the lower panel of Fig. 6, the three stars with lower masses should be conventional NS, and the others could be HNS in our DS2 model.

The observational data of the radius still suffer large uncertainties. In the upper panel we include the sources 4U1820-30 and SAXJ1808.4-3658, whose mass, radius, and spin are available. One can see that according to their small radii both sources should preferably be high-mass compact HNS in our model, whereas their masses in the lower panel identify them as preferably "low-mass" NNS. This can also be seen in Fig. 2, where the same data points are reproduced. However, within their large error bars, both data are still consistent with our model. We expect more accurate observations (in particular precise

radius measurements by future satellite missions NICER, SKA, Athena [88–90]) to constrain our parameters or rule out the model.

### C. Phase transition caused by rotational evolution

The possibility of a phase transition to QM caused by rotational evolution has been widely discussed in the literature [42–45]. For a constant baryonic mass, a rotating star loses its rotation energy by magnetic dipole radiation, which makes the star spin down and the central density increase. When the central density of a NNS reaches a critical value, the phase transition from hadronic matter to QM will take place, and the star converts to a HNS. As the star continues spinning down and the central density continues increasing, more and more QM appears in the core of the HNS.

This is clearly shown in Fig. 7, where we display the change of the number density of all particle species with rotational frequency in the interior of a star with baryonic mass $M_B = 2.0\ M_\odot$ for the DS2 EOS (corresponding to $M = 1.74\ M_\odot$ in the static sequence and $M = 1.80\ M_\odot$ at the Kepler frequency $f_K = 1018$ Hz; see the lower panel of Fig. 5). One notes that this star at Keplerian frequency has no QM core, but as it spins down, it is compressed to a smaller volume, which enhances the central density, and the star is converted into a HNS. As the frequency decreases further, the QM mixed phase extends outward from the core and the region occupied by the pure hadron phase gets narrower. At the same time, the radius of the star is decreasing.

A pure QM phase in the core is never reached in our calculations with the Gibbs construction and $\alpha = 2$. This is at variance with models employing Maxwell constructions, e.g., [30,40,45], which obviously exhibit a very different interior structure. Nevertheless global NS properties like the maximum mass or radius are usually not strongly affected by the type of phase transition employed; see [75,76] for a comparison of different phase transition constructions. We reiterate that both types of phase transitions are idealizations.

In Fig. 8 we present the stellar models with DS2 EOS in the $f$–$M_B$ plane, where the same labels as in Fig. 6 are used; i.e., the dash-dotted lilac curve represents the onset of conversion from a NNS to a HNS. It can be seen that the conversion is possible only in the baryon mass range $1.84 < M_B/M_\odot < 2.37$. Examples could be the pulsars J1903+0327 and 4U1820-30, located at the edge of the phase transition boundary in Fig. 6. Above that range, even the fastest rotating stars are already HNS. In addition, when the star's baryonic mass is larger than 2.35 $M_\odot$, the static configuration is unstable, and the star will collapse to a black hole as it loses angular momentum and meets the SAI borderline (dashed red curve). These are *supramassive* stars [3,49,50] that will be discussed in more detail in the following. The maximum baryonic mass for the DS2 EOS is 2.87 $M_\odot$. The various limits are indicated by vertical lines in Fig. 8.

For further illustration, we show in the upper panel of Fig. 9 the fraction of QM in HNS as a function of the rotation frequency for several choices of fixed baryonic

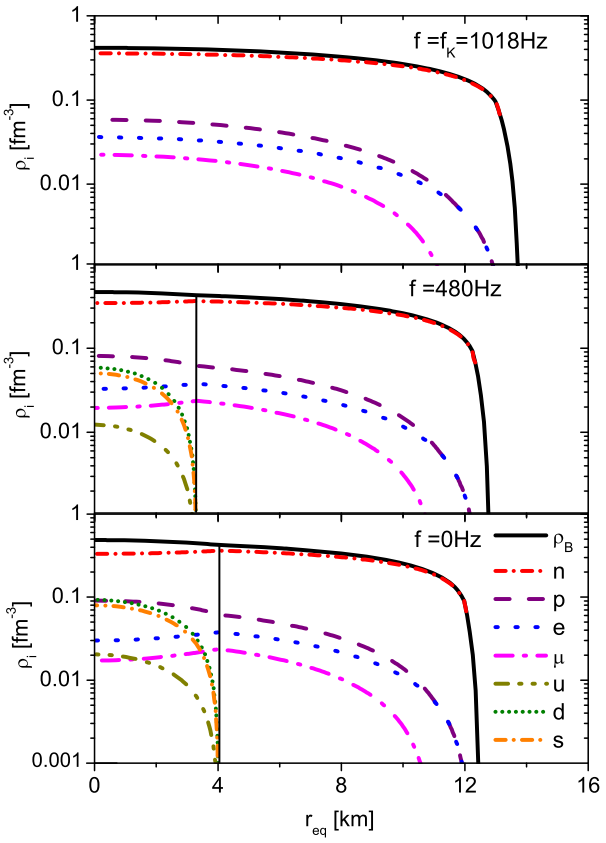


FIG. 7. Equatorial profiles of particle number densities of a rotating NS of baryonic mass $M_B = 2.0\ M_\odot$ at various rotation frequencies with the DS2 EOS. The vertical solid lines represent the interface of the two phases.

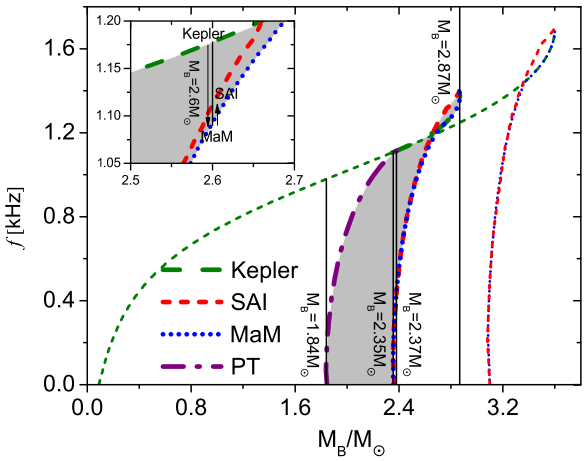


FIG. 8. The allowed domain of HNS with the EOS DS2 in the $f$–$M_B$ plane. The legend is as in Fig. 6.

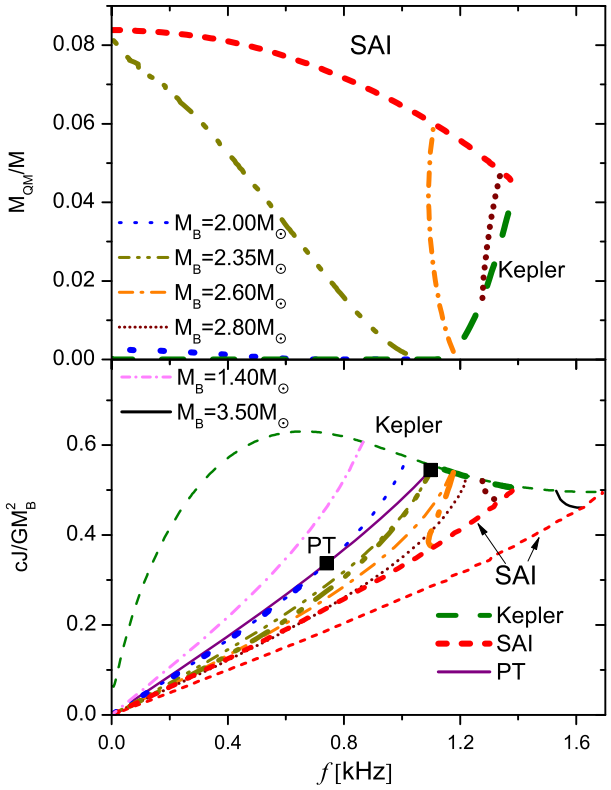


FIG. 9. Mass fraction of QM (upper panel) and angular momentum (lower panel) as a function of rotation frequency for several fixed values of $M_B$. Bold curves are for HNS with the DS2 EOS and thin curves (in the lower plot) represent the results for NNS. The markers indicate the onset of the HQ phase transition. The Kepler, SAI, and PT lines are shown, as in Figs. 6 and 8. Note that all $M_B = 1.40\ M_\odot$ stars (dash-dotted pink curve) and $M_B = 3.50\ M_\odot$ stars (solid black curve) are NNS without QM content.

mass with the DS2 EOS. The trajectories in the $M$–$R_{\rm eq}$ plane for the same values of $M_B$ are reported in Fig. 5. Usually the QM fraction increases with decreasing frequency due to the increasing density and extension of the QM domain in the star; see Fig. 7. The maximum value of 8.39% is reached for the heaviest possible static NS with $M_B = 2.35\ M_\odot$; see Fig. 8. This value can be increased by choosing larger values of $\alpha$ in the DSM, but then the maximum HNS mass falls below two solar masses. Supramassive HNS ($M_B > 2.35\ M_\odot$) have no static limit and collapse when reaching the (dashed red) SAI line. Their QM fraction remains below the maximum static value.

In the lower panel of Fig. 9 we show the angular momentum as a function of rotation frequency for NNS and HNS. The conversion points between NNS and HNS are indicated by markers in some cases. Normal HNS ($M_B < 2.35\ M_\odot$) are spinning down when losing angular momentum in the evolution, whereas supramassive (e.g., $M_B = 2.6\ M_\odot$) stars spin up close to the SAI collapse [49]. A similar backbending phenomenon is often related to the onset of the phase transition from hadronic matter to QM [42,43], but here it only occurs for both HNS and NNS in supramassive configurations close to the collapse, in the case of NNS for $3.10 < M_B/M_\odot < 3.59$; see Fig. 8.

In more detail, for example for the $M_B = 2.6\ M_\odot$ trajectory in Fig. 9, Fig. 5, and the inset of Fig. 8, the HNS spins down until it reaches the minimum of the fixed rotation frequency curve ($f = 1082$ Hz) at the MaM curves (dotted blue curves in Figs. 5 and 8). Then it spins up until the final SAI point. In fact, in the evolution the maximum angular momentum is given at the Kepler sequence and the minimum angular momentum at the static sequence or the SAI line. Therefore, if the lower boundary of the frequency in Fig. 8 is not at the static sequence or the SAI line, i.e., when the MaM lines (dotted blue lines) split from the SAI lines (short-dashed red lines) in Figs. 5, 6, and 8, the loss of angular momentum will cause a spin-up.

Quantitatively, the difference of angular momentum between NNS and HNS with equal baryonic mass and frequency is slight at lower baryon mass ($M_B < 2.35\ M_\odot$), but becomes important for larger masses, where the QM content increases and only HNS exhibit the spin-up phenomenon.

## IV. CONCLUSIONS AND OUTLOOK

We have investigated the properties of rotating hybrid neutron stars, employing an EOS constructed with the BHF approach for nucleonic matter and the Dyson-Schwinger model for quark matter, and assuming the phase transition under the Gibbs construction. We computed the properties of hybrid stars in the Keplerian sequence, respecting the secular axisymmetric instability constraint.

Hybrid stars are more compact and have lower maximum masses and maximum Kepler frequencies than ordinary neutron stars, which would provide a theoretical possibility to exclude the existence of hybrid stars (taking our nucleonic and quark matter EOSs for granted). However, this would require the detection of extremely massive and rapidly rotating stars, whereas for the moment our results for the maximum mass, maximum rotation frequency, and the equatorial radius range of either nucleonic or hybrid stars fulfill the current constraints by observational data of the fastest rotating pulsars.

A more immediate progress could be the future measurement of sufficiently precise neutron star radii or even $M(R)$ relations, which would directly single out or reject EOSs and thus discriminate between pure neutron stars or hybrid stars, for example. In this regard, twin neutron stars require very special conditions, difficult to reconcile with current radius measurements, in particular. They do not exist in our approach.

We also investigated the phase transition induced by the spin-down of pulsars with a constant baryonic mass. We showed the variation of the quark matter content under rotational evolution and found that the quark ratios are

small, with the maximum value about 8%, in order to respect the current two-solar-mass lower limit of the maximum mass. We also found that in our model the spin-up (backbending) phenomenon is not related to the phase transition, but happens in supramassive stars before they collapse to black holes, which is possible in a narrow range of large (but very different) masses for both hybrid stars and normal neutron stars.

All results obviously depend on the chosen nucleonic EOS and the parameters in the Dyson-Schwinger model. For the future it will be important to establish direct estimates of the model parameters in a more fundamental way from QCD, to provide in this way more reliable predictions, and also to clarify the qualitative differences between different current theoretical quark models. Furthermore, the hadron-quark phase transition should be modeled more realistically, taking into account finite-size effects.

## ACKNOWLEDGMENTS

We acknowledge financial support from National Natural Science Foundation of China (Grants No. 11305144, No. 11475149, and No. 11303023), and the Fundamental Research Funds for the Central Universities of China (CUGL 140609). Partial support comes from "NewCompStar," European Cooperation in Science and Technology Action MP1304.

[1] N. K. Glendenning, *Compact Stars, Nuclear Physics, Particle Physics, and General Relativity*, 2nd ed. (Springer, New York, 2000).
[2] P. Haensel, A. Y. Potekhin, and D. G. Yakovlev, *Neutron Stars 1: Equations of State and Structure* (Springer, New York, 2007).
[3] M. Camenzind, *Compact Objects in Astrophysics—White Dwarfs, Neutron Stars and Black Holes* (Springer, New York, 2007).
[4] F. Özel and P. Freire, Annu. Rev. Astron. Astrophys. **54**, 401 (2016).
[5] J. M. Lattimer and M. Prakash, Phys. Rep. **621**, 127 (2016).
[6] D. D. Ivanenko and D. F. Kurdgelaidze, Astrophysics **1**, 251 (1965).
[7] N. Itoh, Prog. Theor. Phys. **44**, 291 (1970).
[8] F. Weber, G. A. Contrera, M. G. Orsaria, G. Milva, W. Spinella, and O. Zubairi, Mod. Phys. Lett. A **29**, 1430022 (2014).
[9] R. B. Wiringa, V. Fiks, and A. Fabrocini, Phys. Rev. C **38**, 1010 (1988).
[10] R. Brockmann and R. Machleidt, Phys. Rev. C **42**, 1965 (1990).
[11] M. Baldo, I. Bombaci, and G. F. Burgio, Astron. Astrophys. **328**, 274 (1997).
[12] A. Akmal, V. R. Pandharipande, and D. G. Ravenhall, Phys. Rev. C **58**, 1804 (1998).
[13] X. R. Zhou, G. F. Burgio, U. Lombardo, H.-J. Schulze, and W. Zuo, Phys. Rev. C **69**, 018801 (2004).
[14] J. R. Stone, J. Phys. G **31**, R211 (2005).
[15] H.-J. Schulze, A. Polls, A. Ramos, and I. Vidana, Phys. Rev. C **73**, 058801 (2006).
[16] Z. H. Li and H.-J. Schulze, Phys. Rev. C **78**, 028801 (2008).
[17] E. Epelbaum, H.-W. Hammer, and Ulf-G. Meissner, Rev. Mod. Phys. **81**, 1773 (2009).
[18] S. Typel, G. Röpke, T. Klähn, D. Blaschke, and H. H. Wolter, Phys. Rev. C **81**, 015803 (2010).
[19] R. Machleidt and D. R. Entem, Phys. Rep. **503**, 1 (2011).
[20] M. Baldo and G. F. Burgio, Rep. Prog. Phys. **75**, 026301 (2012).
[21] N. Kalantar-Nayestanaki, E. Epelbaum, J. G. Messchendorp, and A. Nogga, Rep. Prog. Phys. **75**, 016301 (2012).
[22] M. Oertel, M. Hempel, T. Klähn, and S. Typel, Rev. Mod. Phys. **89**, 015007 (2017).
[23] A. Chodos, R. L. Jaffe, K. Johnson, C. B. Thorn, and V. F. Weisskopf, Phys. Rev. D **9**, 3471 (1974).
[24] M. Buballa, Phys. Rep. **407**, 205 (2005).
[25] T. Klähn, R. Lastowiecki, and D. Blaschke, Phys. Rev. D **88**, 085001 (2013).
[26] T. Klähn and T. Fischer, Astrophys. J. **810**, 134 (2015).
[27] K. Schertler, S. Leupold, and J. Schaffner-Bielich, Phys. Rev. C **60**, 025801 (1999).
[28] Y.-L. Tian, Y. Yan, H. Li, X.-L. Luo, and H.-S. Zong, Phys. Rev. D **85**, 045009 (2012).
[29] T. Zhao, Y. Yan, X.-L. Luo, and H.-S. Zong, Phys. Rev. D **91**, 034018 (2015).
[30] A. Zacchi, R. Stiele, and J. Schaffner-Bielich, Phys. Rev. D **92**, 045022 (2015); A. Zacchi, M. Hanauske, and J. Schaffner-Bielich, Phys. Rev. D **93**, 065011 (2016).
[31] C. D. Roberts and A. G. Williams, Prog. Part. Nucl. Phys. **33**, 477 (1994).
[32] R. Alkofer and L. von Smekal, Phys. Rep. **353**, 281 (2001).
[33] H. Chen, M. Baldo, G. F. Burgio, and H.-J. Schulze, Phys. Rev. D **84**, 105023 (2011); **86**, 045006 (2012).
[34] H. Chen, J. B. Wei, M. Baldo, G. F. Burgio, and H. J. Schulze, Phys. Rev. D **91**, 105002 (2015).
[35] H. Chen, J. B. Wei, and H. J. Schulze, Eur. Phys. J. A **52**, 291 (2016).
[36] R. Schaeffer, L. Zdunik, and P. Haensel, Astron. Astrophys. **126**, 121 (1983).
[37] N. K. Glendenning and C. Kettner, Astron. Astrophys. **353**, L9 (2000).
[38] K. Schertler, C. Greiner, J. Schaffner-Bielich, and M. H. Thoma, Nucl. Phys. **A677**, 463 (2000).

[39] M. G. Alford, S. Han, and M. Prakash, Phys. Rev. D **88**, 083013 (2013); M. G. Alford, G. F. Burgio, S. Han, G. Taranto, and D. Zappalà, Phys. Rev. D **92**, 083002 (2015).
[40] M. Bejger, D. Blaschke, P. Haensel, J. L. Zdunik, and M. Fortin, Astron. Astrophys. **600**, A39 (2017).
[41] A. Zacchi, L. Tolos, and J. Schaffner-Bielich, Phys. Rev. D **95**, 103008 (2017).
[42] N. K. Glendenning, S. Pei, and F. Weber, Phys. Rev. Lett. **79**, 1603 (1997).
[43] P. Haensel, M. Bejger, M. Fortin, and L. Zdunik, Eur. Phys. J. A **52**, 59 (2016).
[44] N. K. Spyrou and N. Stergioulas, Astron. Astrophys. **395**, 151 (2002).
[45] N. S. Ayvazyan, G. Colucci, D. H. Rischke, and A. Sedrakian, Astron. Astrophys. **559**, A118 (2013).
[46] J. W. T. Hessels, S. M. Ransom, I. H. Stairs, P. C. C. Freire, V. M. Kaspi, and F. Camilo, Science **311**, 1901 (2006).
[47] H. Komatsu, Y. Eriguchi, and I. Hachisu, Mon. Not. R. Astron. Soc. **237**, 355 (1989); **239**, 153 (1989).
[48] F. Weber, N. K. Glendenning, and M. K. Weigel, Astrophys. J. **373**, 579 (1991); F. Weber and N. K. Glendenning, Phys. Lett. B **265**, 1 (1991).
[49] G. B. Cook, S. L. Shapiro, and S. A. Teukolsky, Astrophys. J. **398**, 203 (1992); **424**, 823 (1994).
[50] M. Salgado, S. Bonazzola, E. Gourgoulhon, and P. Haensel, Astron. Astrophys. **291**, 155 (1994).
[51] N. Stergioulas and J. L. Friedman, Astrophys. J. **444**, 306 (1995); N. Stergioulas, Living Rev. Relativ. **6**, 3 (2003).
[52] M. Baldo, *Nuclear Methods and the Nuclear Equation of State*, International Review of Nuclear Physics Vol. 8 (World Scientific, Singapore, 1999).
[53] H.-J. Schulze and T. Rijken, Phys. Rev. C **84**, 035801 (2011); Th. A. Rijken and H.-J. Schulze, Eur. Phys. J. A **52**, 21 (2016).
[54] P. B. Demorest, T. Pennucci, S. M. Ransom, M. S. E. Roberts, and J. W. T. Hessels, Nature (London) **467**, 1081 (2010).
[55] J. A. Antoniadis *et al.*, Science **340**, 1233232 (2013).
[56] E. Fonseca *et al.*, Astrophys. J. **832**, 167 (2016).
[57] J. Schaffner-Bielich, Nucl. Phys. **A835**, 279 (2010).
[58] R. Machleidt, K. Holinde, and Ch. Elster, Phys. Rep. **149**, 1 (1987); R. Machleidt, Adv. Nucl. Phys. **19**, 189 (1989).
[59] A. Lejeune and P. Grangé, M. Martzolff, and J. Cugnon, Nucl. Phys. **A453**, 189 (1986); W. Zuo, A. Lejeune, U. Lombardo, and J.-F. Mathiot, Nucl. Phys. **A706**, 418 (2002); Z. H. Li, U. Lombardo, H.-J. Schulze, and W. Zuo, Phys. Rev. C **77**, 034316 (2008).
[60] J. Carlson, V. R. Pandharipande, and R. B. Wiringa, Nucl. Phys. **A401**, 59 (1983); R. Schiavilla, V. R. Pandharipande, and R. B. Wiringa, Nucl. Phys. **A449**, 219 (1986); B. S. Pudliner, V. R. Pandharipande, J. Carlson, S. C. Pieper, and R. B. Wiringa, Phys. Rev. C **56**, 1720 (1997).
[61] M. Alford and S. Reddy, Phys. Rev. D **67**, 074024 (2003).
[62] W. Yuan, H. Chen, and Y.-X. Liu, Phys. Lett. B **637**, 69 (2006).
[63] D. Nickel, J. Wambach, and R. Alkofer, Phys. Rev. D **73**, 114028 (2006); D. Nickel, R. Alkofer, and J. Wambach, Phys. Rev. D **74**, 114015 (2006).
[64] H. Chen, W. Yuan, L. Chang, Y. X. Liu, T. Klähn, and C. D. Roberts, Phys. Rev. D **78**, 116015 (2008).
[65] Y. Jiang, H. Chen, W.-M Sun, and H.-S. Zong, J. High Energy Phys. 04 (2013) 014.
[66] R. Alkofer, P. Watson, and H. Weigel, Phys. Rev. D **65**, 094026 (2002).
[67] L. Chang and C. D. Roberts, Phys. Rev. Lett. **103**, 081601 (2009).
[68] T. Klähn, C. D. Roberts, L. Chang, H. Chen, and Y. X. Liu, Phys. Rev. C **82**, 035801 (2010).
[69] S. X. Qin, L. Chang, H. Chen, Y. X. Liu, and C. D. Roberts, Phys. Rev. Lett. **106**, 172301 (2011).
[70] C. S. Fischer and J. Luecker, Phys. Lett. B **718**, 1036 (2013).
[71] C. S. Fischer, L. Fister, J. Luecker, and J. M. Pawlowski, Phys. Lett. B **732**, 273 (2014).
[72] C. S. Fischer, J. Luecker, and C. A. Welzbacher, Phys. Rev. D **90**, 034022 (2014).
[73] G. Eichmann, C. S. Fischer, and C. A. Welzbacher, Phys. Rev. D **93**, 034013 (2016).
[74] N. K. Glendenning, Phys. Rev. D **46**, 1274 (1992).
[75] T. Maruyama, S. Chiba, H.-J. Schulze, and T. Tatsumi, Phys. Rev. D **76**, 123015 (2007).
[76] H. Chen, G. F. Burgio, H.-J. Schulze, and N. Yasutake, Astron. Astrophys. **551**, A13 (2013).
[77] R. P. Feynman, N. Metropolis, and E. Teller, Phys. Rev. **75**, 1561 (1949).
[78] G. Baym, C. Pethick, and D. Sutherland, Astrophys. J. **170**, 299 (1971).
[79] http://www.gravity.phys.uwm.edu/rns/.
[80] P. Haensel, M. Salgado, and S. Bonazzola, Astron. Astrophys. **296**, 745 (1995).
[81] O. Benhar, V. Ferrari, L. Gualtieri, and S. Marassi, Phys. Rev. D **72**, 044028 (2005).
[82] J. M. Lattimer and M. Prakash, Phys. Rep. **442**, 109 (2007).
[83] P. Haensel, J. L. Zdunik, M. Bejger, and J. M. Lattimer, Astron. Astrophys. **502**, 605 (2009).
[84] N. B. Zhang, B. Qi, S. Y. Wang, S. L. Ge, and B. Y. Sun, Int. J. Mod. Phys. E **22**, 1350085 (2013).
[85] P. Kaaret, Z. Prieskorn, J. J. M. in 't Zand, S. Brandt, N. Lund, S. Mereghetti, D. Götz, E. Kuulkers, and J. A. Tomsick, Astrophys. J. Lett. **657**, L97 (2007).
[86] J. M. Lattimer and M. Prakash, Science **304**, 536 (2004).
[87] A. Kurkela, P. Romatschke, A. Vuorinen, and B. Wu, arXiv: 1006.4062.
[88] https://www.nasa.gov/nicer/; Z. Arzoumanian *et al.*, Proc. SPIE Int. Soc. Opt. Eng. **9144**, 914420 (2014).
[89] http://skatelescope.org/; A. Watts *et al.*, Proc. Sci., AASKA14 (**2015**) 043.
[90] http://www.the-athena-x-ray-observatory.eu/; X. Barcons, K. Nandra, D. Barret, J.-W. den Herder, A. C. Fabian, L. Piro, and M. G. Watson, J. Phys. Conf. Ser. **610**, 012008 (2015).